Synthesis of $KBiO_3$/Nano-Ag_3PO_4 Composite Photocatalyst and Its Application for Degradation of Organic Pollutants under Visible Light

Cheng, Ting
School of Environmental Ecology, Jiangsu City Vocational College, Nanjing, 210036, P.R. CHINA

Chen, Chen*[+]; Ye, Chenhao
School of Environmental and Chemical Engineering, Jiangsu University of Science and Technology Zhenjiang, 212003, P.R. CHINA

Xie, Weifang; Zhang, Xiao[•]
School of Environmental Ecology, Jiangsu City Vocational College, Nanjing, 210036, P.R. CHINA

Tian, Yuan
School of Environmental and Chemical Engineering, Jiangsu University of Science and Technology Zhenjiang, 212003, P.R. CHINA

ABSTRACT: *In this work, a novel composite photocatalyst, $KBiO_3$/nano-Ag_3PO_4 (K/Ag catalyst), was synthesized, and efficiently degraded methylene blue (MB) under visible light. The various properties of photocatalysts were measured by modern analytical techniques, such as XRD, FT-IR, SEM, XPS, and UV-Vis. We also utilized Density functional theory calculation (DFT) to investigate the photocatalytic degradation mechanism in this reaction process. The multiple characterization findings demonstrated that K/Ag composite catalyst was successfully synthesized using Ag_3PO_4 and $KBiO_3$, and it displayed excellent absorption of visible light. The photocatalytic results confirmed that K/Ag catalyst greatly promoted the degradation of MB under visible light. The first-order reaction kinetics model could satisfactorily describe the apparent photocatalytic degradation process in this system. In addition, adding electron capture agents to the photocatalytic system highly decreased the degradation efficiencies of the target pollutant. Moreover, K/Ag composite catalyst exhibited perfect photocatalyst stability after recycling three times. By calculating the band structure, Density of States (DOS), and work function, $KBiO_3$ and Ag_3PO_4 could be considered as n-type and p-type semiconductor materials, respectively. When the composite catalyst was exposed to light, the light-excited electrons would have appeared in both the conduction bands. Furthermore, the transfer trend of electrons and holes made photogenerated electrons concentrate on the conduction band of n-type $KBiO_3$, and photogenerated holes concentrate on the valence band of p-type Ag_3PO_4, thereby greatly improving the photocatalytic efficiency.*

KEYWORDS: *Photocatalysis; Composite photocatalyst; Ag_3PO_4; DFT calculation.*

* *To whom correspondence should be addressed.*
+ *E-mail: chenc@just.edu.cn & chencjust@sina.com*
• *Other Address: Nanjing University and Yancheng Academy of Environmental Technology and Engineering, Yancheng 224000, P.R. CHINA*
1021-9986/2022/6/1942-1960 19/$/6.09

INTRODUCTION

In China, millions of tons of industrial organic wastewater, coming from many chemical industrial production companies, are discharged every year [1, 2]. If this kind of wastewater is treated improperly, it is likely to have serious impacts on the ecological environment and human health. Therefore, effective treatment techniques are essential to decrease the pollution from such wastewater. At present, the treatment methods of organic wastewater mainly include biological treatment [3, 4], the chemical method [5, 6], adsorption [7-9], membrane separation [10, 11], advanced oxidation [12, 13], and photocatalytic degradation [14-16]. Each of these methods has its own advantages, while also exist several shortcomings. For example, biological treatment requires the domestication of microorganisms and strict operating conditions; the cost of the chemical method is very expensive, and the solution remained is likely to produce secondary pollution; the cost of adsorbents is relatively higher in adsorption and the cycle adsorption efficiency is lower; membrane fouling is a common problem in membrane separation techniques. Among these methods, the photocatalytic method is a new water treatment process developed in the last century. Photocatalysis uses the photogenerated electrons and holes produced by photocatalysts under light excitation efficiently oxidize and reduce pollutants [17]. Due to its simple operation, high degradation efficiency, and the recyclability of catalysts, photocatalytic technology has become one of the hot spots in the field of water treatment.

Photocatalyst plays an essential role in photocatalytic technology. The commonly used photocatalysts include TiO_2 [18, 19], ZnO [20-22], $BiVO_4$ [23, 24], ZrO_2 [25, 26], CdS[27, 28], C_3N_4 [29, 30], and so forth. Due to the impact of band gap and band structure, electron-hole recombination efficiency, and other factors, the degradation efficiency of a single photocatalytic material is very limited, so composite photocatalyst materials have attracted the attention of many researchers. The p-n heterojunctions are a common photocatalyst composite method [31, 32]. Generally speaking, for a typical p-n heterojunction, the Fermi level of p-type photocatalyst is close to the top of the valence band, while that of n-type photocatalyst is near the bottom of the conduction band. When the p-type catalyst and n-type catalyst are composed together, that could effectively promote the separation of photogenerated electrons and holes. In this case, it can reduce the probability of electron/hole recombination, and improve the photocatalytic efficiency.

Ag_3PO_4 is considered to be an efficient photocatalytic material. It has an excellent absorption of visible light due to its band gap (2.4eV) [33, 34]. Ag_3PO_4 is also used as a p-type photocatalyst by many researchers. According to related literature, Mohaghegh prepared Ag_3PO_4/$BiPO_4$ p-n heterojunction nano-composite material, and the photocatalytic activity for phthalocyanine reactive blue 21 was improved compared to pure Ag_3PO_4 and $BiPO_4$ [35]. Zhang constructed p-n type Ag_3PO_4/$CdWO_4$ heterojunction photocatalyst and used it for visible-light-induced dye degradation [36]. Wang synthesized p-n heterojunction Ag_3PO_4/$NaTaO_3$ composite photocatalyst, and visible-light-driven photocatalytic performance for Rhodamine B dye molecules was enhanced [37]. Through Density Functional Theory (DFT) calculation, Reunchan concluded that Ag_3PO_4 was a p-type semiconductor material [38], and *Huang et al*. obtained similar research results [39]. In addition, $KBiO_3$ (band gap is 2.1ev) is one of the bismuth photocatalytic materials. The photocatalytic properties of $KBiO_3$ have been proved in research [40-42], and it is considered an n-type photocatalyst material [41]. Moreover, Ag_3PO_4 and $KBiO_3$ belong to p-type and n-type photocatalyst materials, respectively. They exhibit obvious band gap differences. So far, the composite photocatalyst prepared by Ag_3PO_4 and $KBiO_3$ has not been reported in the literatures, and the photocatalytic performances exhibited in organic substances were also not illustrated yet. Theoretically speaking, the p-n heterojunction composite photocatalyst synthesized by Ag_3PO_4 and $KBiO_3$ is likely to achieve the effective migration of photo-generated electrons and holes between two catalysts, and the enhancement of photocatalytic performance is expected under visible light.

In this work, the preparation and synthesis of $KBiO_3$/Nano-Ag_3PO_4 composite photocatalyst （K/Ag catalyst）were reported. To prove the various properties and electronic structure, the composite photocatalyst material was characterized by X-Ray Diffraction (XRD), Fourier Transforms InfraRed (FT-IR) spectroscopy, Scanning Electron Microscopy-energy dispersive (SEM) spectroscopy, X-ray Photoelectron Spectroscopy (XPS), UV-Vis diffuse reflectance spectra, and so on. We also conducted the VASP software and DFT

the calculation to further investigate the action of photogenerated holes, and deeply clarify the photocatalytic mechanism. The photocatalytic efficiency of K/Ag catalyst was evaluated by photocatalysis degradation experiments of methylene blue in solution. The impact factors, including reaction time, and reaction kinetics, were also investigated. Moreover, the recycling usage of K/Ag catalysts in photocatalytic systems was discussed. Furthermore, the photocatalytic reaction mechanism was studied through DFT calculation. The experiment and theoretical calculation results proved that K/Ag catalyst exhibited excellent photocatalytic activity for the degradation of organic pollutants in solution.

EXPERIMENTAL SECTION

Synthesis of photocatalysts

$KBiO_3$ was prepared using the roasting method. In the experiment, the reaction between KOH and $NaBiO_3.2H_2O$ were carried out under the mole ratio of 2:1. Firstly, the KOH and $NaBiO_3.2H_2O$ were weighted and grounded together in a solid mixture using agate mortar. Then, the solid mixture was roasted in a muffle furnace at 250℃ for 2 hours. After that, the sample was washed with distilled water many times until its neutral, then dried at under 80℃ to constant weight.

Ag_3PO_4 was prepared using the precipitation method. Firstly, 2g of PVP (polyvinyl pyrrolidone) was added to 200mL of distilled water, and then 2.4g of $AgNO_3$ was dissolved in the solution. Secondly, 0.84g of Na_2HPO_4 was dissolved in distilled water, and mixed with PVP-$AgNO_3$ aqueous solution. Thirdly, the above mixture was stirred for 1 hour by a magnetic stirrer, and centrifuged by a Low-speed benchtop centrifuge. Finally, the precipitation was washed with ethanol and dried at the temperature of 80℃ to constant weight.

The preparation process of K/Ag composite photocatalyst mainly includes the following steps. Firstly, prepare the $KBiO_3$ using the above process. Secondly, add 2g PVP into 200mL distilled water, and continue to mix and dissolve 2.4g $AgNO_3$ in the solution. Thirdly, put 0.84g Na_2HPO_4 in distilled water, and then mix with 1.39g $KBiO_3$ and PVP-$AgNO_3$ aqueous solution. After that, stir the mixture for 3 hours, and then centrifuge. After that, stand the mixture for 3 hours, and wash it with ethanol many times. Finally, the samples were dried at 80℃ to constant weight.

Photocatalytic experiments

Photocatalytic experiments and their efficiency were evaluated by degrading Methylene blue under visible light irradiation (300W Xe-lamp). In each experiment, 0.020g of the photocatalyst was put in 50mL solution of MB (the initial concentration was 20mg/L). A transparent photoreaction vessel was utilized to put in the mixture samples, and all experiments were performed at room temperature. In addition, the reaction time of photocatalytic reactions ranged from 0 to 240mins. After the reaction was over, the residual concentration of MB was measured by an ultraviolet-visible spectrophotometer. Besides, the TOC and COD values were measured in the photodegradation process of K/Ag composite photocatalyst. The TOC was determined by Metash TOC-3000 total organic carbon analyzer, and the COD was determined by the national standard 11914-89 chemical oxygen demand measurement method. In the COD and TOC degradation experiments, the initial concentration of MB was 100mg/L, COD was 165mg/L, and TOC was 82mg/L. In the COD and TOC degradation experiments, 0.1g of the photocatalyst was put in 50mL solution. Moreover, to investigate the degradation mechanism of the photocatalytic reaction, different trapping agents, such as EDTA-2Na, TBA (*tert*-butyl alcohol), BQ (1,4-benzoquinone), and CCl_4, were put into the reaction mixtures. To further evaluate the reuse performance of the photocatalyst, K/Ag catalyst was filtered out from the solution by 0.45μm filter membrane. And then, the filer solids were washed with distilled water many times until its neutral, then dried at 80 ℃ with air blowing thermostatic oven.

Materials characterization

To investigate the photocatalytic properties of this material, samples synthesized were characterized by modern analytical instruments, including X-ray fluorescence, X-ray diffraction, Fourier transform infrared spectroscopy, Scanning electron microscopy-energy dispersive spectroscopy, X-Ray photoelectron spectroscopy, Microiontophoresis apparatus, UV-Vis diffuse reflectance spectra, Xigo Liquid specific surface area Determinator, Malvern Mastersizer 2000 Laser particle size analyzer, and so forth. ARL-9800 X-ray fluorescence analyzer (Swiss ARL) was used to analyze X-Ray fluorescence; Shimadzu XD-3A diffractometer was used to measure XRD patterns of powder photocatalyst,

with Cu-Kα radiation (λ = 1.54056Å); HITACHI(S-3400N) scanning electron microscope was utilized to observe the morphologies of composite catalyst; Nicolet iS5 FT-IR spectrometer was exploited to record the FT-IR spectra of samples; PHI 5000 VersaProbe XPS instrument was utilized to draw the X-ray photoelectron spectroscopy spectra; PerkinElmer Ultraviolet spectrophotometer was exploited to measure the UV-Vis spectrum. The Liquid specific surface area of K/Ag composite catalyst was analyzed through Xigo Liquid-specific surface area Determinator. Moreover, the particle size distribution was measured by Malvern Mastersizer 2000 Laser particle size analyzer.

DFT calculation

To further investigate the photocatalytic mechanism in the reaction process, the DFT calculation was performed via Vienna Ab initio Simulation Package (VASP) software [43] and spin-polarized Density Functional Theory (DFT). The exchange-correlation potential was calculated by Perdew-Burke-Ernzerhof (PBE) [44, 45] functional within the generalized gradient approximation (GGA) method [46, 47]. In addition, the cut-off energy for the calculation is 450eV, and the K-points grids of dimensions were 5×5×5. Moreover, the crystal model of Ag_3PO_4 and $KBiO_3$ (as shown in Fig.1a and Fig.1b, respectively) were exploited to calculate the Band structure and Density of States (DOS). Using the surface model of Ag_3PO_4 and $KBiO_3$ (as shown in Fig.1c and Fig.1d, respectively), we calculated the work function.

The vacuum slab for the surface model was designed as 35Å for Ag_3PO_4 and 15 Å for $KBiO_3$. In the calculation process, we optimized the atomic coordinates and cell parameters of Ag_3PO_4 and $KBiO_3$. In theory, the model structure of Ag_3PO_4 and $KBiO_3$ are cell units, including 2P, 6Ag, 8O atoms, and 12K, 12Bi, and 36O atoms, respectively.

RESULTS AND DISCUSSIONS

Particle size distribution and liquid-specific surface area

Fig.2 depicted the particle size distribution (Fig.2a) and liquid-specific surface area (Fig.2b) results of K/Ag composite catalyst. It was observed from Fig.2a that the particle size distribution of K/Ag composite catalyst presented a bimodal structure, suggesting that the material contained two substances. Combined with other analysis techniques, we believed that the particles in the range of 0.04μm to 0.5μm were mainly Ag_3PO_4, and the particles distributed in the range of 0.5μm to 20μm were mainly $KBiO_3$ particles. In addition, Fig.2b depicted the analytical results of the liquid-phase surface area for K/Ag composite catalyst. According to the fitting calculation of instrument software, the liquid-specific surface area of K/Ag Catalyst was about 344m^2/g.

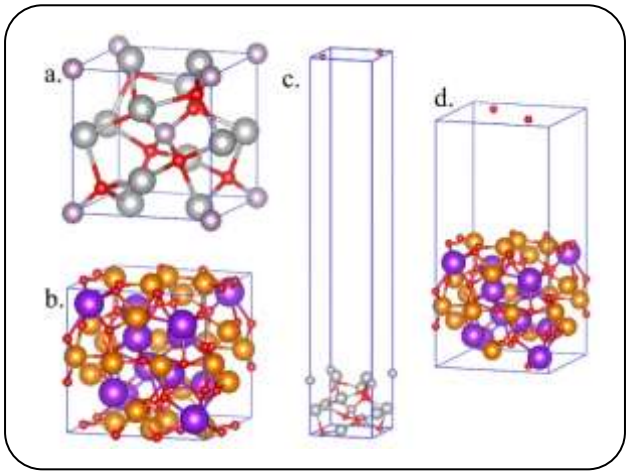

Fig. 1: The theory structure of crystal model Ag_3PO_4 (a), $KBiO_3$ (b) and theory structure of surface model Ag_3PO_4 (c), $KBiO_3$ (d) (grey ball is Ag atom, the lavender ball is P atom, the red ball is O atom, the orange ball is Bi atom, the purple ball is K atom).

XRD

The XRD curves of Ag_3PO_4, $KBiO_3$, and K/Ag composite catalyst were depicted in Fig.3. It was observed that the primary peaks of Ag_3PO_4 could appear at 2θ, 20.71º, 29.45º, 33.01º, 36.26º, 42.13º, 47.37º, 52.21º, 54.52º, and 56.76º. These peaks were in agreement with the standard peaks of PDF#06-0505. In addition, the primary peaks of $KBiO_3$ appeared at 2θ, 12.54º, 17.78º, 21.82º, 28.30º, 31.02º, 33.60º, 46.62º, 55.24º, and 56.90º, which could be ascribed to the standard peaks of PDF#47-0879. Moreover, in XRD curves of K/Ag composite catalyst, chief peaks of pure Ag_3PO_4 and $KBiO_3$ could be observed. These findings indicated that K/Ag composite catalyst was successfully synthesized utilizing Ag_3PO_4 and $KBiO_3$ in the synthesis reaction.

FT-IR

To investigate the molecular functional groups of K/Ag composite catalyst, we utilized the Fourier transform infrared spectroscopy to analyze its infrared absorption

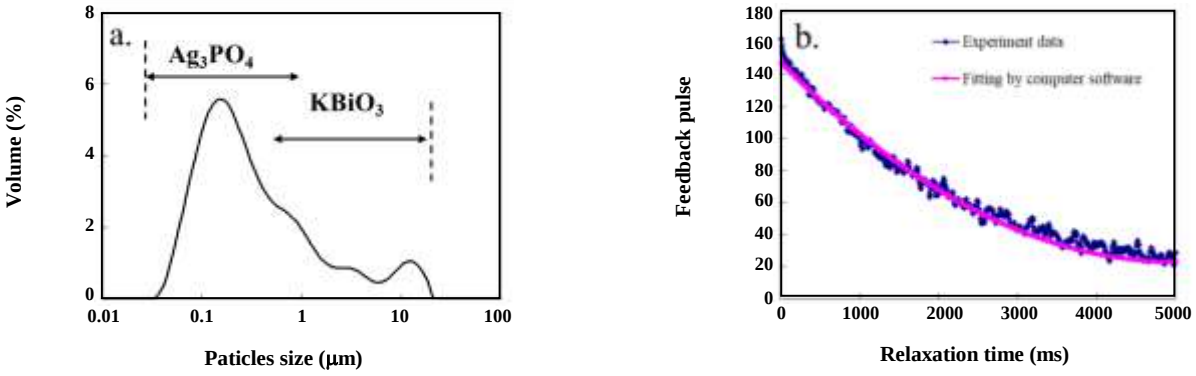

Fig. 2: Particle size distribution and liquid-specific surface area results of K/Ag composite catalyst.

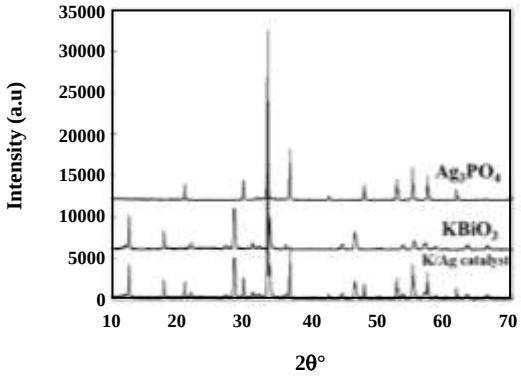

Fig. 3: XRD patterns of Ag_3PO_4, $KBiO_3$, and K/Ag catalyst.

spectrum (Fig.4c). Meanwhile, the spectrums of both Ag_3PO_4 and $KBiO_3$ are analyzed as comparisons (Fig.4a and Fig.4b). Among curves of these three samples, the strong and broad peaks around 3450cm^{-1} to 2900 cm^{-1}, and 1670 cm^{-1} to 1684 cm^{-1}, could be observed. These peaks belonged to the stretching and bending vibration of O–H [48, 49]. That might be the adsorbed water and crystal water in the samples. In addition, we could observe the stretching and bending vibrations of PO_4^{3-} at around 560cm^{-1} and 1036 cm^{-1} in curves of Ag_3PO_4 [50]. The peaks around 1411cm^{-1}, 848cm^{-1}, 562cm^{-1}, and 489cm^{-1} should be ascribed to the O–Bi–O bending mode in curves of $KBiO_3$ [40, 41]. What's more, we observed that typical peaks of Ag_3PO_4 and $KBiO_3$ (1417cm^{-1}, 1066cm^{-1}, 845cm^{-1}, 560cm^{-1}, and 491cm^{-1}) appeared in the spectra of K/Ag composite catalyst. Furthermore, there was a little position shift and deformation of typical peaks in curves, which might be ascribed to the change in synthesis conditions. These findings implied that K/Ag composite catalyst could be regarded as the compound of Ag_3PO_4 and $KBiO_3$.

UV–Vis diffuse reflectance spectra

Fig.5 depicted the curves of UV-Vis diffuse reflectance spectra for Ag_3PO_4, $KBiO_3$, and K/Ag catalysts. The broad absorption bands of Ag_3PO_4 and $KBiO_3$, around 500nm and 750nm, could be observed in Fig.4, which indicated that $KBiO_3$ had better visible light absorption than that Ag_3PO_4. In addition, there were similarities in the absorption band between K/Ag catalyst and $KBiO_3$. This phenomenon suggested that K/Ag catalyst was likely to exhibit acceptable visible light absorption performance. Besides, it was observed that the adsorption edge of K/Ag catalyst slightly moved to the direction of lower wavelength compared with that of $KBiO_3$, and the shift of spectrum might mainly ascribe to the lower adsorption edge of Ag_3PO_4.

Moreover, the Tauc equation (as below) is often used to calculate the band gap energy[51].

$$\alpha(\nu)h\nu = A(h\nu - Eg)^{n/2} \quad [52, 53] \quad (1)$$

Where, *α, h, v, A,* and *Eg* represent absorption coefficient at light frequency v, Planck constant, light frequency, a constant, and band gap energy, respectively. For direct transition semiconductor as Ag_3PO_4 and $KBiO_3$, the value of n is 1.

According to the Tauc equation, the value of Eg could be obtained by fitting the curve of $[a(v)hv]^2$ versus *hv*, and extrapolating the linear part of the curve to zero absorption coefficient. Through the analysis and calculation, the band

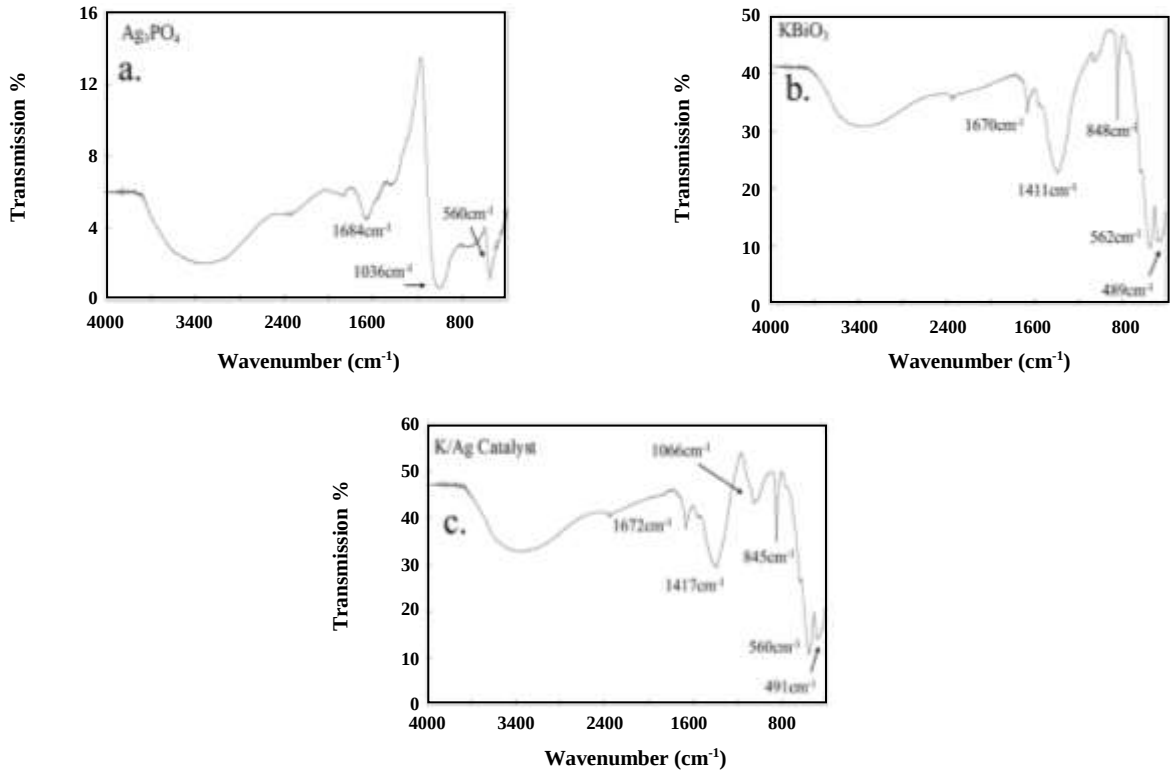

Fig. 4: FT-IR spectra of Ag_3PO_4 (a), $KBiO_3$ (b) and K/Ag Catalyst (c).

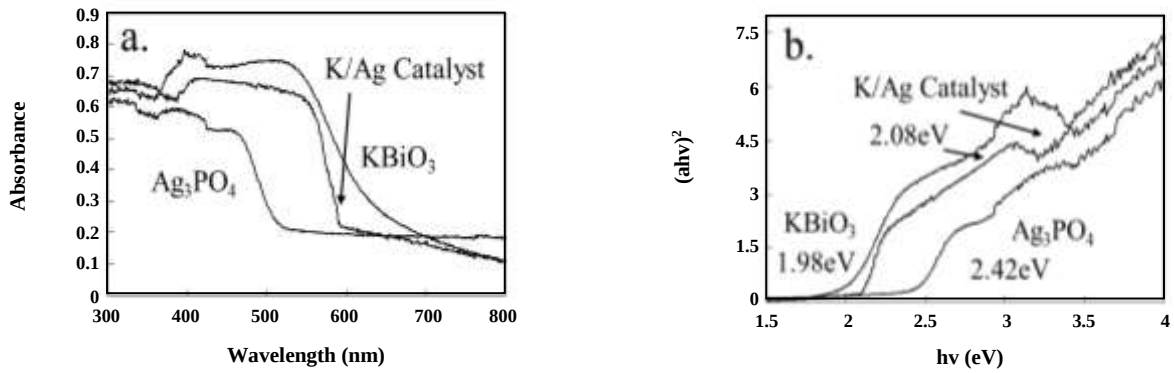

Fig. 5: UV-Vis diffuse reflectance spectra of Ag_3PO_4, $KBiO_3$, and K/Ag Catalyst.

gaps energy and its corresponding curves were gained in Fig.4b. The band gaps energy of Ag_3PO_4 and $KBiO_3$ were 2.42eV and 1.98eV, respectively. These findings were very close to the results of other literature [37, 41]. Besides, the band gap energy of K/Ag catalyst was 2.08eV, which was between the values of Ag_3PO_4 and $KBiO_3$. Meanwhile, the band gap energy of 2.08eV also pointed out that K/Ag catalyst displayed excellent absorption properties for visible light.

SEM-EDX

We also analyzed the morphology and EDX of K/Ag catalyst, and the results were shown in Fig.6. It is observed that K/Ag catalyst exhibited amorphous morphology, and it consisted of two types of particles with different particle sizes. EDX results (area 1 in Fig.6a) displayed that the main chemical composition (atomic percent/%) of the catalyst was around 22.3%Ag, 7.1%P, 7.4%Bi, 6.1%K, and 56.1%O

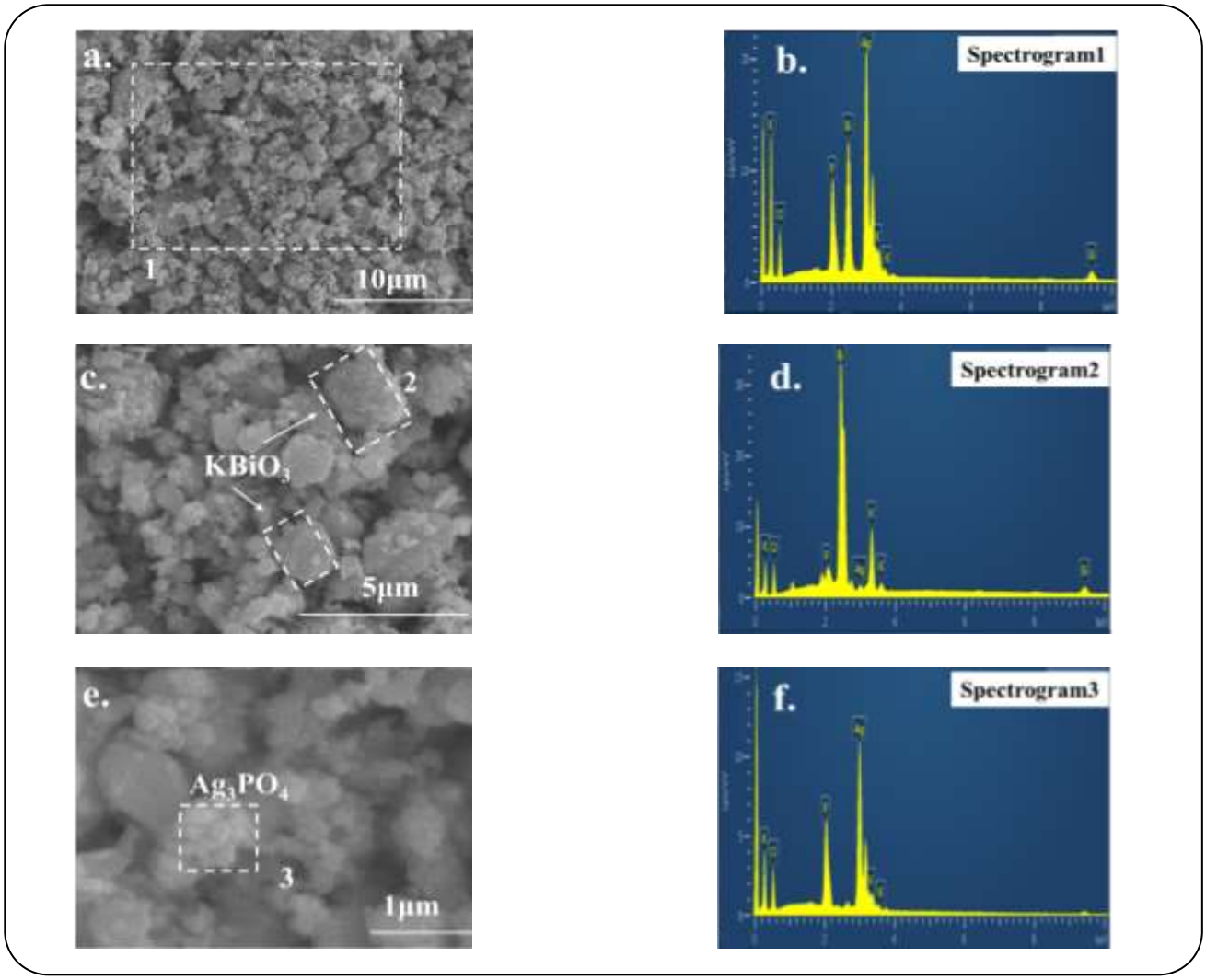

Fig. 6: The morphology of K/Ag catalyst（a, c, and e）and EDS results (b, d, and f).

(Fig.6b), and these findings were in line with that of other characterization techniques.

It could be observed from Fig.6c and Fig.6e that the size of bigger particles ranged from 2μm to 5μm. The EDS analysis results (area 2 and area 3) revealed that the main compositions (atomic percent/%) of bigger particles were 23.3% Bi, 22.2% K, 51.3% O, and trace Ag and P. Accordingly, it is determined that the large particles were $KBiO_4$. Moreover, Fig.6 showed that the small particles of the catalyst had a size of 250nm to 500nm, and such nano-sized particles might greatly accelerate their photocatalytic activity. Furthermore, according to the chemical composition (36.2%Ag, 11.5%P, 51.2%O, and trace K), given by EDX and the morphology, the small particles were identified as Ag_3PO_4, which was in accordance with other research [50, 54]. From Fig.6c and Fig.6e, we also observed that Ag_3PO_4 and $KBiO_3$ were tightly integrated, which might be conducive to the transfer of light-excited electrons and holes. It was worth mentioning that, the transformation of electrons and holes between Ag_3PO_4 and $KBiO_3$ was likely to greatly improve the photocatalytic performance. Consequently, according to the analysis of SEM-EDX and other previous characterization techniques, we confirmed that the composite catalyst of Ag_3PO_4 and $KBiO_3$ were synthesized successfully.

XPS

Fig. 7 further evaluated the surface chemical composition of K/Ag catalyst, analyzed by XPS. It could be seen that the main peaks of K/Ag catalyst appeared

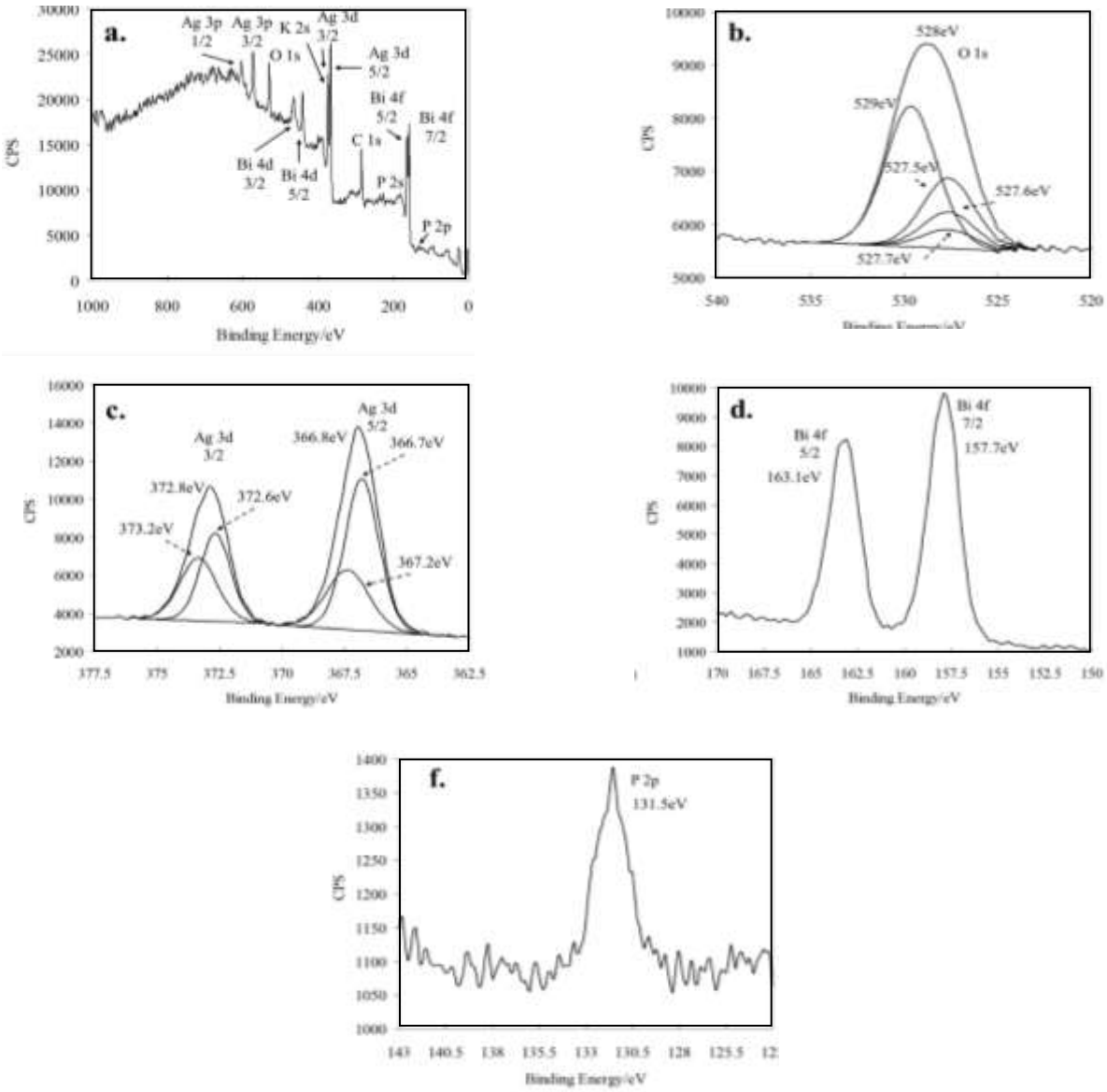

Fig. 7: The wide scan XPS spectra of K/Ag catalyst(a); the high-resolution XPS spectra of O1s (b); Ag3d (c); Bi4f (d) and P2p (f).

were C1s (283eV), O1s (529eV), Ag3d (367eV and 373eV), Ag3p (572eV and 602eV), Bi4f (158eV and 163eV), Bi4d (440eV and 464eV), and P2p (131.5eV). Except for the carbon element (testing needs), all the other elements could be found in Ag_3PO_4 and $KBiO_3$, and that was in line with the analysis of other previous characterization methods. In addition, more details could be obtained from the high-resolution XPS spectra of O1s and Ag3d. The binding energy of O1s appeared at 528eV, and this positive binding energy shift might be explained to the bonds between O and other elements.

Moreover, the O1s peak consisted of four individual peaks, 529eV, 527.5eV, 527.6eV, and 527.7eV, which may be ascribed to Ag-O/P-O bond in Ag_3PO_4 molecule, K-O and Bi-O bond in $KBiO_3$ molecule, respectively. Fig.7c depicted that both Ag $3d_{5/2}$ and Ag $3d_{3/2}$ peaks could consist of two individual peaks at 366.7eV, 367.2eV, 372.6eV, and 373.2eV. The peak splitting should be ascribed to the different existing forms of Ag in Ag_3PO_4 and $KBiO_3$ [55, 56]. Besides, the two new peaks of Bi4f at 163.1eV and 157.7eV corresponded to $Bi4f_{5/2}$ and $Bi4f_{7/2}$ in Fig.7d, and they might derive from the characteristics

Table 1: Comparison of the catalytic ability of K/Ag catalyst with other latest photocatalytic materials.

	MB concentration (mg/L)	90min C_t/C_0
K/Ag catalyst	20	about 18%
Ag decorated g-C_3N_4/$LaFeO_3$ [59]	10	about 5%
CdS/SnO_2 heterostructured nanoparticle [60]	about 6.4	about 50%
AgNPs@ZIF-8 composite [61]	about 32	about 10%
mesoporous $BiVO_4$ photocatalyst [63]	20mg/L	all degraded
g-C_3N_4/MnV_2O_6 heterojunction [62]	10mg/L	about 22%
Ag decorated g-C_3N_4/$LaFeO_3$ [59]	10mg/L	about 5%

of Bi^{3+} cations in $KBiO_3$ molecule [57, 58]. Additionally, Fig.7f displayed the high-resolution XPS spectra of P2p. The peak of P2p could be observed at 131.5eV, which was in agreement with the widely accepted 2p atom orbit of the P element. In conclusion, XPS spectra analytical results further confirmed the existing elements and their existing forms in the K/Ag catalyst.

Photocatalytic activity

Generally speaking, photocatalytic experiments could be used to evaluate the performance of photocatalysts for the degradation of organic pollutants. To verify the photocatalytic properties of the composite K/Ag catalyst synthesized, we conducted experiments to degrade MB under visible light, and the results were showed in Fig.8. In the process of experiments, the Xe lamp was turned on at 0 min. In the reaction stage within 20 min, MB and catalyst are contacted completely, which could be favored the degradation of the target pollutant. In Fig.8a, it is obvious that the degradation effect of MB under K/Ag photocatalytic system was greatly promoted than that of the pure Ag_3PO_4 and $KBiO_3$ system. For instance, the residual rate of MB was 3.3% at 240min in K/Ag catalyst system, while the residual rate in Ag_3PO_4 and $KBiO_3$ systems were 58.5% and 34.9%, respectively. These results proved that the composite catalyst of Ag_3PO_4 and $KBiO_3$ exhibited clear photocatalytic activity. Additionally, the degradation effect of K/Ag photocatalytic system was comparable to some of the other photocatalytic materials, including Ag decorated g-C_3N_4/$LaFeO_3$[59], CdS/SnO_2 heterostructured nanoparticle[60], AgNPs@ZIF-8 composite[61], g-C_3N_4/MnV_2O_6 heterojunction[62] and Ag decorated g-C_3N_4/$LaFeO_3$[59]. Its photocatalytic ability was slightly weaker than mesoporous $BiVO_4$ photocatalyst[63]. Change of the UV-Visible absorption spectrum of MB with reaction time was depicted in Fig.8b. It suggested that peaks of MB decreased gradually with the increase of reaction time, which indicated that MB was photo-degraded under K/Ag catalyst system.

In addition, we investigated the apparent degradation kinetics in K/Ag photocatalytic system *via* a first-order reaction model[64]. The pure Ag_3PO_4 and $KBiO_3$ systems were also evaluated as comparisons, respectively. The equation of the first-order reaction model is as follows[65]. The reaction constant k can be obtained by fitting equation (2) and the related experimental results[66].

$$\mathrm{Ln}\left(\frac{C}{C_0}\right) = -kt \quad (2)$$

Where, C_0 represents the initial concentration of MB, and C_t represents the concentration of MB at time t.

Fig.8c presented the results of apparent kinetics fitting results utilizing equation (2) (based on the data in Fig.8a) in three systems. According to the literature, the first-order reaction model (equation 2) has been successfully used in the analysis of the apparent kinetics of a variety of new photocatalytic materials, including MoS_2/ZnO heterostructures [67], transition metal doped TiO_2 [68], Cu(II)-Na(I) heterometallic coordination compounds [69] and g-C_3N_4/MnV_2O_6 heterojunction [62].

In the fitting results, the R^2 values of these systems were all above 0.95, which indicated that the first-order reaction model could satisfactorily express the apparent photocatalytic degradation process. Besides, from the k value calculated in Fig.8d, the value of K/Ag catalyst system (0.0143) was the largest, and that was higher than the other two systems.

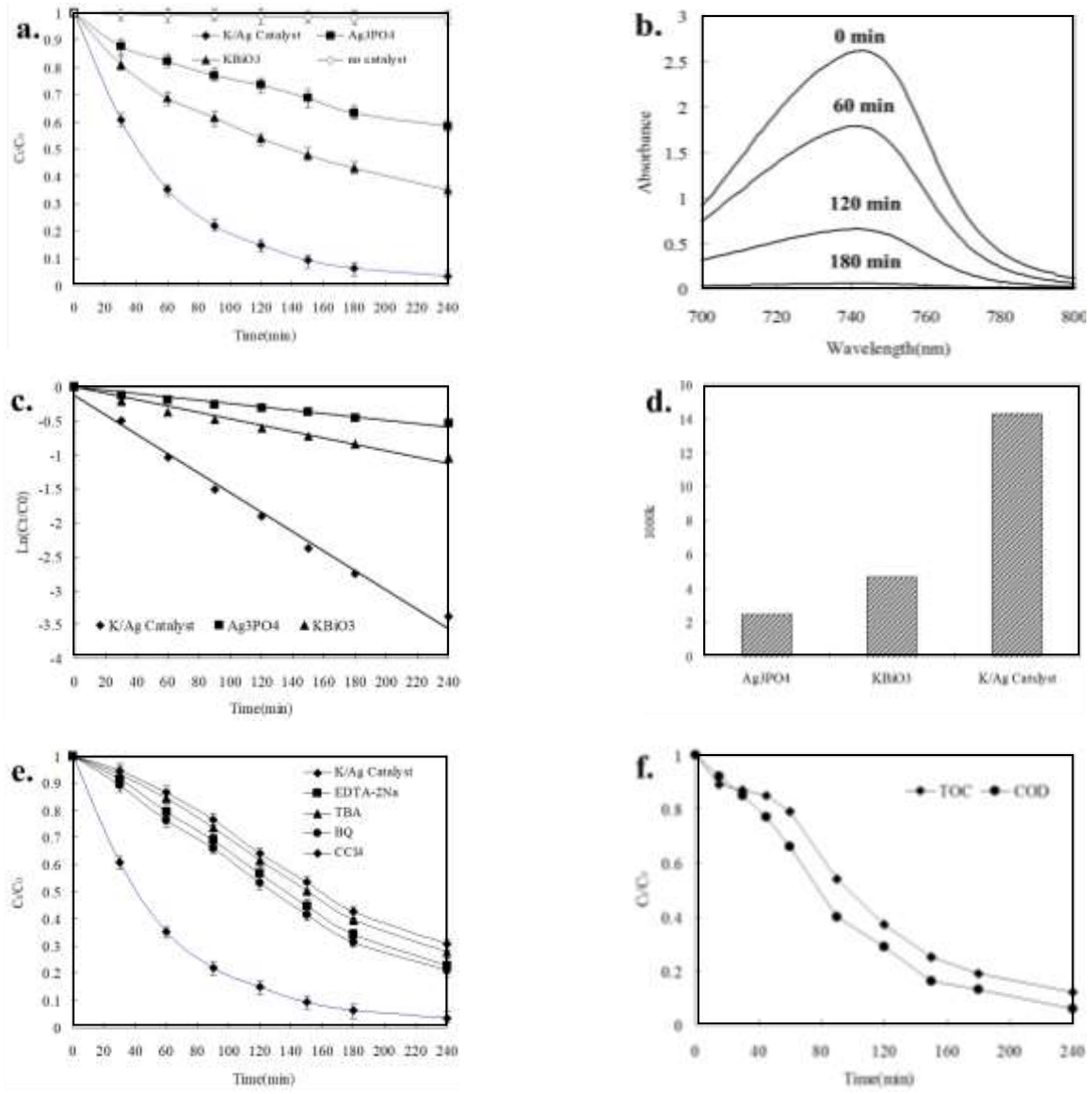

Fig. 8: (a) Photodegradation process of Ag_3PO_4, $KBiO_3$, and K/Ag catalyst; (b) UV-Visible absorption spectrum of MB solution degraded by K/Ag catalyst; (c) the apparent kinetics fitting results using the first-order reactions; (d) the constants of the first-order reactions for MB photodegradation; (e) the effect of trapping agents on the photocatalytic degradation of MB; (f) TOC and COD photodegradation process of K/Ag catalyst.

$$O_2 + e^- \rightarrow \cdot O_2^- \quad (3)$$

$$\cdot O_2^- + MB \rightarrow Degradation - products \quad (4)$$

$$H_2O/OH^- + h^+ \rightarrow \cdot OH^- \quad (5)$$

Theoretically speaking, the strong redox of free electrons, holes, and related free radicals released by photocatalytic catalysts, are crucial to the photocatalytic process. If adding electron capture agents to the photocatalytic system, we can evaluate which active substances play major roles in the process of photocatalysis.

Fig.8e depicted the impact of different trapping agents on the photocatalytic degradation of MB. The related references [70] pointed out, EDTA-2Na, TBA (*tert*-butyl alcohol), BQ (1,4-benzoquinone), and CCl_4 were all electron capture agents. In addition, EDTA-2Na was considered as a hole trapper, TBA was believed

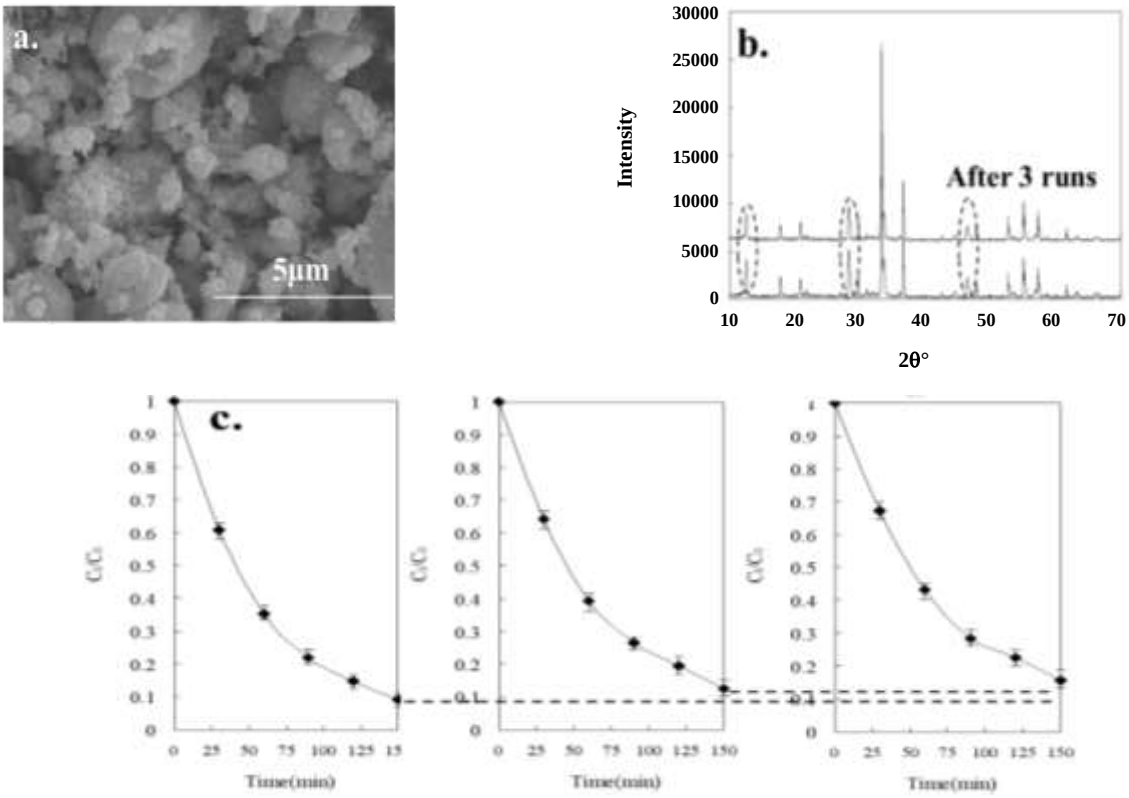

Fig. 9: (a) The morphology of K/Ag catalyst after 3rd photocatalysis experiment ; (b) The XRD patterns of K/Ag catalyst before and after 3rd photocatalysis experiment; (c) The degradation curve of K/Ag catalyst reuse.

as a hydroxyl radical trapper, BQ was known as an oxygen-free radical trapper, and CCl_4 was regarded as an electron trapper. We observed that the photocatalytic degradation efficiencies of K/Ag catalyst were decreased in all systems after adding trapping agents. These findings indicated the degradation paths (as Equations (3) to (5)) might happen during the photocatalytic degradation process of MB. Moreover, among electron capture agents, EDTA-2Na and TBA exhibited a greater impact on the photocatalytic degradation of MB. Besides, the effects of four trappers on the photocatalytic degradation efficiency were generally similar. For instance, at the reaction time of 30 min, the residual rate of MB in the non-trapping agent system was 60.7%, while that of 91.4%, 93.2%, 89.2%, and 94.5% in EDTA-2Na, TBA, BQ, and CCl_4 system, respectively. Also, at the reaction time of 120min, the residual rate of MB in non-trapping agent was only 14.8%, while that of 56.7%, 61.7%, 53.2%, and 64.2% in EDTA-2Na, TBA, BQ, and CCl_4 system, respectively. These results demonstrated that the capture of holes, hydroxyl radicals, BQ, and CCl_4 might seriously affect the degradation activity of pollutants in the photocatalytic system, which could be explained by the main degradation path of MB described in equations (3) to (5).

Fig.8f depicted the change of TOC and COD values in solution with degradation time in K/Ag Catalyst degradation system. It was observed that in the early photocatalytic reaction from 0 to 60min, the concentration of TOC and COD only decreased by about 21% and 34%, respectively, although the concentration of MB decreased by about 65%. This indicated in the early stage of the photocatalytic reaction, MB was not completely degraded into small organic molecules or inorganic substances (such as CO_2 and H_2O), and its degradation intermediates were still organic, which made the degradation efficiency of TOC and COD not high. As the photocatalytic reaction proceeded from 20 min to 240min, the intermediates of MB degradation were further decomposed into organic small molecular substances and inorganic substances, and the values of TOC and COD were rapidly reduced.

Catalysts Recycling

The recycling use of catalysts is also an important indicator for photocatalytic materials. In this experiment, we investigated the photocatalytic degradation effect of the target pollutant after the catalyst was recycled 3 times. Meanwhile, the morphology of the catalyst was evaluated after the photocatalytic reaction experiment, and these findings were displayed in Fig.9. In addition, Fig.9a depicted the morphology of K/Ag catalyst after 3rd photocatalytic reaction experiment. It could be seen that compared with the original catalyst (Fig.6), the catalyst recycled maintained amorphous status, and no obvious changes could be observed in the overall appearance of K/Ag catalyst particles. Besides, Fig.9b depicted XRD patterns of K/Ag catalyst recycled 3 times. Compared with the previous results, the peaks of Ag_3PO_4 and $KBiO_3$ also could be found in the XRD pattern. However, the peak intensities of $KBiO_3$ (2θ at 12.54º, 28.30º, and 46.5º) became a little weaker after 3rd photocatalysis experiment, which might be ascribed to the loss of $KBiO_3$ during the process of photocatalysis reaction. Additionally, we measured the stability and reuse efficiency of K/Ag catalyst after recycling (Fig.9c). There was no obvious attenuation of photocatalytic activity for the catalyst after three times of reuse, and the K/Ag catalyst exhibited excellent photocatalyst stability. Moreover, the photo corroded in the photocatalytic degradation process could be accepted.

Mechanism of photocatalytic reaction

To investigate the degradation mechanism of composite K/Ag catalyst in the process of photocatalysis, we utilized VASP software to study the photocatalytic materials based on the density functional theory, and the results were displayed in Fig.10 to Fig.12. It could be seen that Fig.10 depicted the band structure, density of states, and work function calculated results of $KBiO_3$ material. The band gap of $KBiO_3$ calculated by VASP was 1.78 eV, which was less than the experimental value of 1.98 eV. Such attenuation was considered to be caused by the theoretical defects of density functional theory, and it would not have much impact on the theoretical analysis. In addition, the band system from 1.78eV to 1.98eV indicated that $KBiO_3$ material exhibited excellent absorption of visible light. Moreover, we could observe that the Fermi energy level of $KBiO_3$ material fell in the upper position between the top of the valence band and the bottom of the conduction band. Consequently, $KBiO_3$ could be considered an n-type semiconductor material, and these findings were in agreement with other literature [41]. Besides, it could be seen that the DOS result was inconsistent with that of the band gap. The band gap was around 1.78eV, and the Fermi energy level was right in the middle of the band system. Furthermore, from the work function calculation results are shown in Fig.8c, the vacuum energy level of $KBiO_3$ was 3.94 eV, and the Fermi energy level was -1.49 eV, which indicated that the work function of $KBiO_3$ was 2.45 eV.

Fig.11 described the band structure, the DOS, and the work function calculated results of Ag_3PO_4 material. Compared with the calculated findings of $KBiO_3$, the band gap of Ag_3PO_4 calculated by VASP software was 2.12eV, which was also obviously less than the experimental value of 2.42eV. Again, the band gap from 2.12eV to 2.42eV suggested that Ag_3PO_4 also exhibited eminent absorption for visible light. Besides, the Fermi energy level of Ag_3PO_4 material was lower in the middle of the band gap (Fig.11a). Such results indicated Ag_3PO_4 had the properties of p-type semiconductor material. These findings were also in line with other research [35-37]. Additionally, similar results could be obtained from the DOS results of Ag_3PO_4 in Fig.10b. Moreover, Fig.11c described the work function calculated curves of Ag_3PO_4 material. We could observe that the vacuum energy level of Ag_3PO_4 material was 0.019 eV, the Fermi energy level was -3.98 eV, and its work function was 3.98 eV.

Fig.12 analyzed the changes in the band structure at the interface between Ag_3PO_4 and $KBiO_3$ in the composite process. Fig.12a showed the energy band comparison of Ag_3PO_4 and $KBiO_3$ materials before the composition. When the vacuum energy level of the two materials was 0, the Fermi energy level for Ag_3PO_4 material was -3.96eV, which was lower than that of -1.49 eV for $KBiO_3$ material. Moreover, combined with the calculated findings of band structure displayed in Fig.10 and Fig.12, we could calculate that the conduction band bottom of Ag_3PO_4 material was -2.3093 eV, and the valence band top was -4.4293 eV. Also, the conduction band bottom of $KBiO_3$ material was -0.6292, and the valence band top was -2.498 eV. Besides, there was only a small amount of crossover between the energy bands of the two materials.

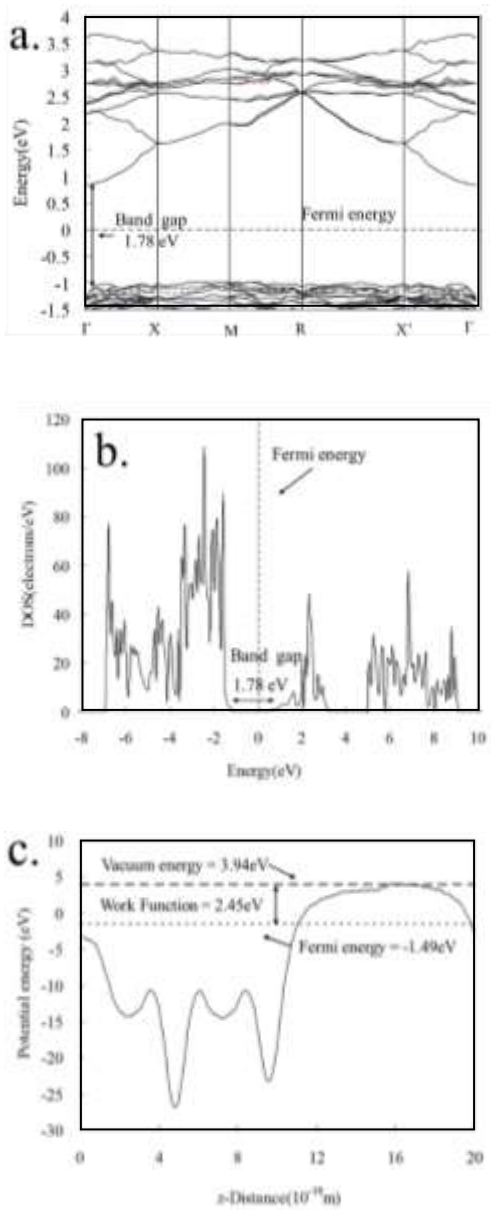

Fig. 10: The band structure, DOS, and work function calculated curves of $KBiO_3$.

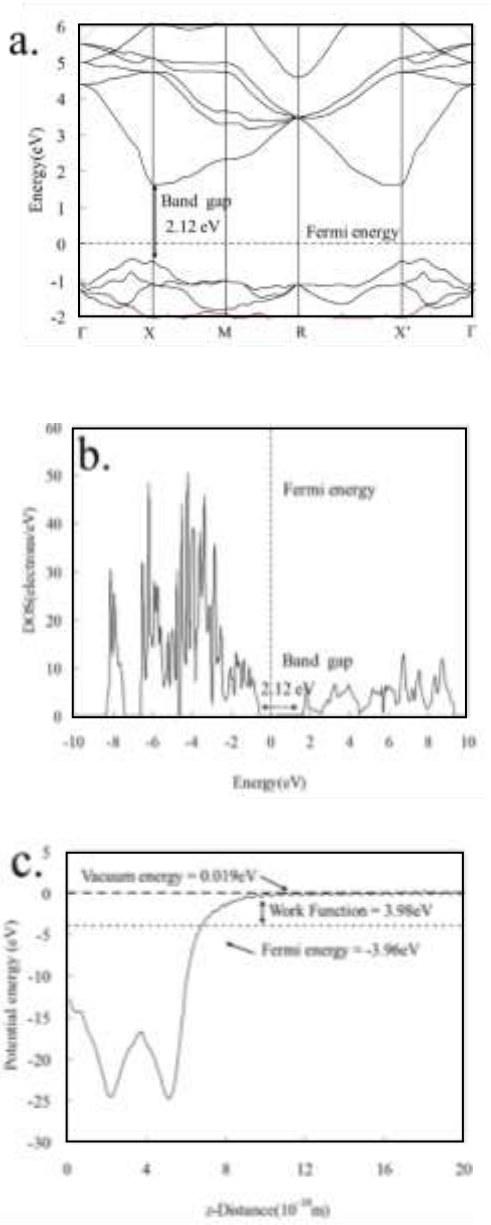

Fig. 11: The band structure, DOS and work function calculated curves of Ag_3PO_4.

According to the classic p-n heterojunction theory, when the interface between p-type Ag_3PO_4 and n-type $KBiO_3$ material is contacted, the electrons in the n-type $KBiO_3$ were transferred to p-type Ag_3PO_4 material. This phenomenon was due to the hole effect caused by the difference in the concentration of electrons and holes between these two materials. Meanwhile, the holes in p-type Ag_3PO_4 would also transfer to n-type $KBiO_3$ material. Such internal transfer of electron and hole would cause the increase of Fermi energy level for p-type Ag_3PO_4 and the decrease for n-type $KBiO_3$. When the Fermi energy levels of two materials reached the same position, they might reach an equilibrium as shown in Fig.10c. At the same time, an internal electric field might be formed from n-type $KBiO_3$ to p-type Ag_3PO_4 at the interface between the two materials. When the composite material was exposed to light, the light-excited electrons would appear in both the conduction bands, since both Ag_3PO_4 and $KBiO_3$ materials had excellent

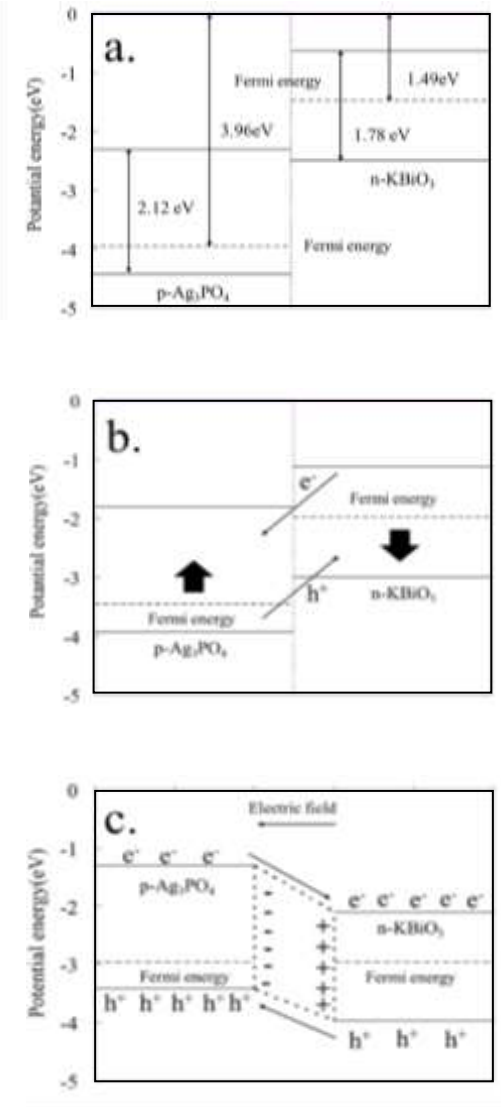

Fig. 12: The photocatalytic mechanism of composite K/Ag catalyst.

absorption for visible light and the corresponding holes should be appeared both in the valence band.

Furthermore, under the action of the internal electric field at the interface, the photo-generated electrons on the conduction band of Ag_3PO_4 would be transferred to the conduction band of $KBiO_3$, and the photo-generated holes in the valence band of $KBiO_3$ would also transfer to Ag_3PO_4 under the same electric field simultaneously. Such transfer trend of electrons and holes made photo-generated electrons concentrate on the conduction band of n-type $KBiO_3$, and photo-generated holes concentrate

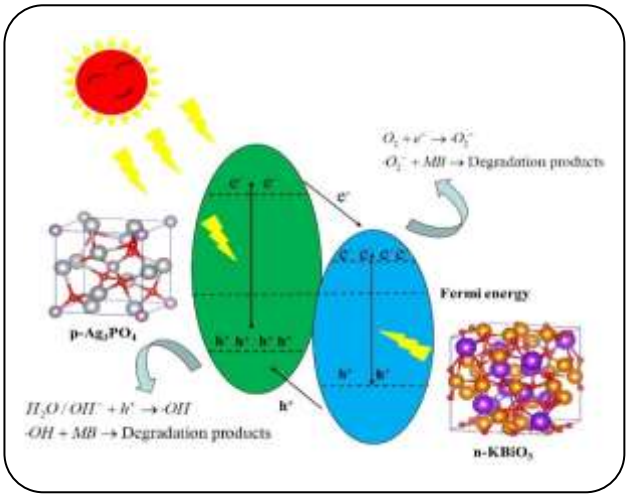

Fig. 13: Schematic diagram of degradation process by composite K/Ag catalyst under visible light.

on the valence band of p-type Ag_3PO_4. In this way, it reduced the recombination probability of photo-generated electrons and holes and enhanced the separation between them. Thereby, the photocatalysis efficiency was likely to be improved effectively. It was worth noting that, if the photo-generated holes accumulated in the valence band of Ag_3PO_4 diffuse to the surface of the material, they would oxidize organic pollutants directly, or react with water to produce highly reactive hydroxyl radicals. Similarly, the electrons accumulated on the conduction band of $KBiO_3$ would diffuse to the surface of the material, and directly reduce organic pollutants, or react with dissolved oxygen to generate oxygen-free radicals. These reactions based on equations from (3) to (5) could effectively degrade organic matter in the reaction system (as shown in Fig. 13).

CONCLUSIONS

A composite photocatalyst, $KBiO_3$/nano-Ag_3PO_4, was synthesized, characterized, and applied to the photocatalytic degradation of MB. The catalyst was characterized by XRD, FT-IR, SEM, XPS, UV-Vis, and so on. The analytical results confirmed that K/Ag composite catalyst was successfully synthesized, and exhibited favorable absorption for visible light. The DFT calculation was utilized to illustrate the photocatalytic degradation mechanism. The photocatalytic experiments results suggested that K/Ag composite catalyst displayed excellent photocatalytic activity under visible light, and it accelerated the degradation of MB effectively. The photocatalytic degradation process could be satisfactorily expressed by the first-order reaction kinetics model.

Besides, after adding the electron capture agents to the photocatalytic reaction system, the degradation efficiencies of MB were reduced greatly. Moreover, after recycling use three times, the K/Ag composite catalyst still maintained highly photocatalytic activity and stability. Furthermore, the calculation of band structure, DOS, and work function illustrated that $KBiO_3$ could be considered as the n-type semiconductor material and Ag_3PO_4 as a p-type semiconductor material. There was an internal transfer of electrons and a hole between $KBiO_3$ and Ag_3PO_4, which would increase the Fermi energy level of Ag_3PO_4 and decrease that of $KBiO_3$. The light-excited electrons would appear in the conduction bands of two materials when the composite catalyst was exposed to light, which accordingly highly accelerated the photocatalytic efficiency of the target pollutant. These findings demonstrated that K/Ag composite catalyst obtained great potential in the photocatalytic degradation of organic pollutants.

Acknowledgments

This work is supported by the Science Foundation of Jiangsu Colleges and Universities (Grant No. 17KJD610001, 17KJD610002); 2021 Jiangsu University Students Innovation and Entrepreneurship Training Program Project; Jiangsu Open University School-level Scientific Research Institutions.

Received : Mar. 27, 2021 ; Accepted : Jul. 19, 2021

REFERENCES

[1] Chen K.-H., Wang H.-C., Han J.-L., Liu W.-Z., Cheng H.-Y., Liang B., Wang A.-J., The Application of Footprints for Assessing the Sustainability of Wastewater Treatment Plants: A Review, *J. Clean. Prod.*, **277**: 124053 (2020).

[2] Yang F., Wang D., Zhao L., Wei F., Efficiency Evaluation for Regional Industrial Water Use and Wastewater Treatment Systems in China: A Dynamic Interactive Network Slacks-Based Measure Model, *J. Environ. Manage.*, **279**: 111721-111721 (2020).

[3] Soh Y.N.A., Kunacheva C., Menon S., Webster R.D., Stuckey D.C., Comparison of Soluble Microbial Product (SMP) Production in Full-Scale Anaerobic/Aerobic Industrial Wastewater Treatment and a Laboratory Based Synthetic Feed Anaerobic Membrane System, *Sci. Total Environ.*, **754**: 142173-142173 (2021).

[4] Zhang W., Tang M., Li D., Yang P., Xu S., Wang D., Effects of Alkalinity on Interaction between EPS and Hydroxy-Aluminum with Different Speciation in Wastewater Sludge Conditioning with Aluminum Based Inorganic Polymer Flocculant, *J. Environ. Sci.*, **100**: 257-268 (2021).

[5] Ma J., Xia W., Zhang R., Ding L., Kong Y., Zhang H., Fu K., Flocculation of Emulsified Oily Wastewater by Using Functional Grafting Modified Chitosan: The Effect of Cationic and Hydrophobic Structure, *J. Hazard Mater*, **403**: 123690-123690 (2021).

[6] Kovacic A., Gys C., Gulin. M.R., Gornik T., Kosjek T., Heath D., Covaci A., Heath E., Kinetics and Biotransformation Products of Bisphenol F and S During Aerobic Degradation with Activated Sludge, *J. Hazard. Mater.*, **404(Pt A)**: 124079-124079 (2021).

[7] Cheng T., Chen C., Tang R., Han C.-H., Tian Y., Competitive Adsorption of Cu, Ni, Pb, and Cd from Aqueous Solution onto Fly Ash-Based Linde F(K) Zeolite, *Iran. J. Chem. Chem. Eng.(IJCCE)*, **37(1)**: 61-72 (2018).

[8] Chen C., Cheng T., Wang Z.L., Han C.H., Removal of Zn^{2+} in Aqueous Solution by Linde F (K) Zeolite Prepared from Recycled Fly Ash, *J. Indian. Chem. Soc.*, **91(2)**: 285-291 (2014).

[9] Chen C., Cheng T., Shi Y., Tian Y., Adsorption of Cu(II) from Aqueous Solution on Fly Ash Based Linde F(K) Zeolite, *Iran. J. Chem. Chem. Eng. (IJCE)*, **33(3)**: 29-35 (2014).

[11] Li T., Ren Y., Wu D., Zhang W., Shi M., Ji C., Lv L., Hua M., Zhang W., A Novel Water-Stable Two-Dimensional Zeolitic Imidazolate Frameworks Thin-Film Composite Membrane for Enhancements in Water Permeability and Nanofiltration Performance, *Chemosphere*, **261**: 127717 (2020).

[12] Zuo S., Jin X., Wang X., Lu Y., Zhu Q., Wang J., Liu W., Du Y., Wang J., Sandwich Structure Stabilized Atomic Fe Catalyst for Highly Efficient Fenton-Like Reaction at All pH Values, *Appl. Catal. B-Environ.*, **282**: 119551 (2021).

[13] Lei D., Xue J., Peng X., Li S., Bi Q., Tang C., Zhang L., Oxalate Enhanced Synergistic Removal of Chromium(VI) and Arsenic(III) over $ZnFe2O_4$/g-C_3N_4: Z-Scheme Charge Transfer Pathway and Photo-Fenton Like Reaction, *Appl. Catal. B-Environ.*, **282**: 119578 (2021).

[14] Zatloukalova K., Obalova L., Koci K., Capek L., Matej Z., Snajdhaufova H., Ryczkowski J., Slowik G., Photocatalytic Degradation of Endocrine Disruptor Compounds in Water over Immobilized TiO_2 Photocatalysts, *Iran. J. Chem. Chem. Eng. (IJCCE)*, **36(2)**: 29-38 (2017).

[15] Mirhoseini F., Salabat A.R., Investigation of Operational Parameters on the Photocatalytic Activity of a New Type of Poly(methyl methacrylate)/Ionic Liquid-TiO_2 Nanocomposite, *Iran. J. Chem. Chem. Eng. (IJCCE)*, **38(4)**: 101-114 (2019).

[16] Malekhosseini H., Mahanpoor K., Khosravi M., Motiee F., Kinetic Modeling and Photocatalytic Reactor Designed for Removal of Resorcinol in Water by Nano $ZnFe_2O_4$/Copper Slag as Catalyst: Using Full Factorial Design of Experiment, *Iran. J. Chem. Chem. Eng. (IJCCE)*, **38(3)**: 257-266 (2019).

[17] Ji Q., Cheng X., Wu Y., Xiang W., He H., Xu Z., Xu C., Qi C., Li S., Zhang L., Yang S., Visible Light Absorption by Perylene Diimide for Synergistic Persulfate Activation Towards Efficient Photodegradation of Bisphenol A, *Appl. Catal. B-Environ.*, **282**: 119579 (2021).

[18] Muhammad B., Bibi A., Javed A., Irfana S., Adnan M., Shah S.H., Khan U.A., Effects of Solvent on the Structure and Properties of Titanium Dioxide Nanoparticles and Their Antibacterial Activity, *Iran J. Chem. Chem. Eng. (IJCCE)*, **38(4)**: 261-272 (2019).

[19] Kachbouri S., Elaloui E., Moussaoui Y., The Effect of Surfactant Chain Length and Type on the Photocatalytic Activity of Mesoporous TiO_2 Nanoparticles Obtained *via* Modified Sol-Gel Process, *Iran. J. Chem. Chen. Eng. (IJCCE)*, **38(1)**: 17-26 (2019).

[20] Zeng P., Yu H., Chen M., Xiao W., Li Y., Liu H., Luo J., Peng J., Shao D., Zhou Z., Luo Z., Wang Y., Chang B., Wang X., Flower-like ZnO Modified with BiOI Nanoparticles as Adsorption/Catalytic Bifunctional Hosts for Lithium-Sulfur Batteries, *J. Energy Chem.*, **51**: 21-29 (2020).

[21] Ramu A.G., Yang D.J., Al Olayan E.M., AlAmri O.D., Aloufi A.S., Almushawwah J.O., Choi D., Synthesis of Hierarchically Structured T-ZnO-rGO-PEI Composite and their Catalytic Removal of Colour and Colourless Phenolic Compounds, *Chemosphere*, **267**: 129245 (2020).

[22] Ekthammathat N., Thongtem S., Thongtem T., Phuruangrat A., Characterization and Antibacterial Activity of Nanostructured ZnO Thin Films Synthesized Through a Hydrothermal Method, *Powder Technol*, **254**: 199-205 (2014).

[23] Fakhravar S., Farhadian M., Tangestaninejad S., Excellent Performance of a Novel Dual Z-Scheme $Cu_2S/Ag_2S/BiVO_4$ Heterostructure in Metronidazole Degradation in Batch and Continuous Systems: Immobilization of Catalytic Particles on Alpha-Al2O3 Fiber, *Appl. Surf. Sci.*, **505**: 144599 (2020).

[24] Yu X., Li H., Hao X., Zhang Z., Wang Y., Li J., Wang Z., Guo C., The Preparation of Ag/Pd/m-$BiVO_4$ Microsphere Photocatalysts with Different Loading Modes and Their Catalytic Activity for Selective Oxidation of Benzyl Alcohol Under Visible Light Irradiation, *Catal. Lett.*, **150(12)**: 3447-3454 (2020).

[25] Wahba M.A., Yakout S.M., Mohamed W.A.A., Galal H.R., Remarkable Photocatalytic Activity of Zr Doped ZnO and ZrO_2/ZnO Nanocomposites: Structural, Morphological and Photoluminescence Properties, *Mater. Chem. Phys.*, **256**: 123754 (2020).

[26] Castro Honorio L.M., Menezes de Oliveira A.L., da Silva Filho E.C., Osajima J.A., Hakki A., Macphee D.E., Garcia dos Santos I.M., Supporting the Photocatalysts on ZrO_2: An Effective Way to Enhance the Photocatalytic Activity of $SrSnO_3$, *Appl. Surf. Sci.*, **528**: 146991 (2020).

[27] Meng X., Yao L., Shi L., Zhang Y., Cui L., Fabrication of 0D/2D CdS/$Bi_{12}O_{17}Cl_2$ Heterojunction Photocatalyst with Boosted Photocatalytic Performance, *Mat. Sci. Semicon. Proc.*, **121**: 105411 (2021).

[28] Wang K., Xing Z., Du M., Zhang S., Li Z., Pan K., Zhou W., Hollow $MoSe_2$@Bi_2S_3/CdS Core-Shell Nanostructure as Dual Z-Scheme Heterojunctions with Enhanced Full Spectrum Photocatalytic-Photothermal Performance, *Appl. Catal. B-Environ.*, **281**: 119482 (2021).

[29] Shi W., Liu C., Li M., Lin X., Guo F., Shi J., Fabrication of Ternary $Ag_3PO_4/Co^{-3}(PO_4)(2)$/g-$C_3N_4$ Heterostructure with Following Type II and Z-Scheme Dual Pathways for Enhanced Visible-Light Photocatalytic Activity, *J. Hazard Mater.*, **389**: 121907 (2020).

[30] Zhang Q., Chen P., Chen L., Wu M., Dai X., Xing P., Lin H., Zhao L., He Y., Facile Fabrication of Novel Ag_2S/K-g-C_3N_4 Composite and Its Enhanced Performance in Photocatalytic H-2 Evolution, *J. Colloid. Interf. Sci.*, **568**: 117-129 (2020).

[31] Li Y., Shen J., Quan W., Diao Y., Wu M., Zhang B., Wang Y., Yang D., 2D/2D p-n Heterojunctions of $CaSb_2O6$/g-C(3)N(4)for Visible Light-Driven Photocatalytic Degradation of Tetracycline, *Eur. J. Inorg. Chem.*, **2020(40)**: 3852-3858 (2020).

[32] He R., Xue K., Wang J., Yan Y., Peng Y., Yang T., Hu Y., Wang W., Nitrogen-Deficient g-C_3Nx/POMs Porous Nanosheets with P-N Heterojunctions Capable of the Efficient Photocatalytic Degradation of Ciprofloxacin, *Chemosphere*, **259**: 127465 (2020).

[33] Alhokbany N.S., Mousa R., Naushad M., Alshehri S.M., Ahamad T., Fabrication of Z-Scheme Photocatalysts g-C3N4/Ag3PO4/Chitosan for the Photocatalytic Degradation of Ciprofloxacin, *Int. J. Biol. Macromol.*, **164**: 3864-3872 (2020).

[34] Yin H., Cao Y., Fan T., Zhang M., Yao J., Li P., Chen S., Liu X., In Situ Synthesis of Ag_3PO_4/C_3N_5 Z-Scheme Heterojunctions with Enhanced Visible-Light-Responsive Photocatalytic Performance for Antibiotics Removal, *Sci. Total. Environ.*, **754**: 141926 (2021).

[35] Mohaghegh N., Rahimi E., Gholami M.R., Ag_3PO_4/$BiPO_4$ p–n Heterojunction Nanocomposite Prepared in Room-Temperature Ionic Liquid Medium with Improved Photocatalytic Activity, *Mat. Sci. Semicon. Proc.*, **39**: 506-514 (2015).

[36] Zhang C., Wang L., Yuan F., Meng R., Chen J., Hou W., Zhu H., Construction of p-n Type Ag_3PO_4/$CdWO_4$ Heterojunction Photocatalyst for Visible-Light-Induced Dye Degradation, *Appl. Surf. Sci.*, **534**: 147544 (2020).

[37] Wang X., Ma J., Kong Y., Fan C., Peng M., Komarneni S., Synthesis of p-n Heterojunction Ag_3PO_4/$NaTaO_3$ Composite Photocatalyst for Enhanced Visible-Light-Driven Photocatalytic Performance, *Mater Lett*, **251**: 192-195 (2019).

[38] Reunchan P., Umezawa N., Native Defects and Hydrogen Impurities in Ag_3PO_4, *Phys. Rev. B*, **87(24)**: 245205 (2013).

[39] Huang Y., Ma T., Chen Q.Y., Cao C., He Y., The Electronic Properties of Impurities (N, C, F, Cl, and S) in Ag_3PO_4: A Hybrid Functional Method Study, *Sci. Rep.*, **5**: 12750 (2015).

[40] Lv F.Z., Hu C.H., Wang D.H., Zhao W., Wei S., Zhong Y., Zhou H.Y., Doping Effect from Ag and Sb in $KBiO_3$ Photocatalyst: First Principles Study, *Mater. Res. Innov.*, **18(sup4)**: S4-1031-S4-1035 (2014).

[41] Zhang H., Zheng H., Wang Y., Yan R., Luo D., Jiang W., KBiO3 as an Effective Visible-Light-Driven Photocatalyst: Stability Improvement by In Situ Constructing $KBiO_3$/BiOX (X = Cl, Br, I) Heterostructure, *Ind. Eng. Chem. Res.*, **58(5)**: 1875-1887 (2019).

[42] Takei T., Haramoto R., Dong Q., Kumada N., Yonesaki Y., Kinomura N., Mano T., Nishimoto S., Kameshima Y., Miyake M., Photocatalytic Activities of Various Pentavalent Bismuthates under Visible Light Irradiation, *J. Solid. State. Chem.*, **184(8)**: 2017-2022 (2011).

[43] Kresse G., Furthmuller J., Efficient Iterative Schemes for ab Initio Total-Energy Calculations Using a Plane-Wave Basis Set, *Phys. Rev. B*, **54(16)**: 11169-11186 (1996).

[44] Hohenberg P., Kohn W., InhomogeIIeous Electron Gas, *Phys Rev*, **136(3B)**: 864-871 (1964).

[45] Kohn W., Sham L.J., Self-Consistent Equations Including Exchange and Correlation Effects, *Phys. Rev.*, **140**: A1133 (1965).

[46] Perdew J., Burke K., Ernzerhof M., Generalized Gradient Approximation Made Simple, *Phys. Rev. Lett.*, **77**: 3865-3868 (1996).

[47] Perdew J.P., Chevary J.A., Vosko S.H., Jackson K.A., Pederson M.R., Singh D.J., Fiolhais C., Atoms, Molecules, Solids, and Surfaces: Applications of the Generalized Gradient Approximation for Exchange and Correlation, *Phys. Rev. B.*, **46**: 6671-6687 (1992).

[48] Zhang X., Cheng T., Chen C., Wang L., Deng Q., Chen G., Ye C., Synthesis of a Novel Magnetic Nano-Zeolite and its Application as an Efficient Heavy Metal Adsorbent, *Mater. Re.s Express.*, **7(8)**: 085007 (2020).

[49] Chen C., Li Q., Shen L., Zhai J., Feasibility of Manufacturing Geopolymer Bricks Using Circulating Fluidized Bed Combustion Bottom Ash, *Environ. Technol.*, **33(10-12)**: 1313-1321 (2012).

[51] Akhtar J., Tahir M.B., Sagir M., Bamufleh H.S., Improved Photocatalytic Performance of Gd and Nd co-Doped ZnO Nanorods for the Degradation of Methylene Blue, *Ceram. Int.*, **46(8)**: 11955-11961 (2020).

[52] Raja A., Rajasekaran P., Vishnu B., Selvakumar K., Yeon Do J., Swaminathan M., Kang M., Fabrication of effective Visible-Light-Driven Ternary Z-Scheme ZnO-Ag-$BiVO_4$ Heterostructured Photocatalyst for Hexavalent Chromium Reduction, *Sep. Purif. Technol.*, **252**: 117446 (2020).

[53] Kim D., Yong K., Boron Doping Induced Charge Transfer Switching of a C_3N_4/ZnO Photocatalyst from Z-Scheme to Type II to Enhance Photocatalytic Hydrogen Production, *Appl. Catal. B-Environ*, **282**: 119538 (2021).

[54] Ramachandran R.., Sathiya M., Ramesha K., Prakash A.S., Madras G., Shukla A.K., Photocatalytic Properties of $KBiO_3$ and $LiBiO_3$ with Tunnel Structures, *J. Chem. Soc.*, **123(4)**: 517-524 (2011).

[55] C. Du., Song. J., Tan S.., Yang L., Yu G., Chen H., L. Zhou., Z. Zhang., Y. Zhang., Y. Su., X. Wen., S. Wang, Facile Synthesis of Z-Acheme ZnO/Ag/Ag_3PO_4 Composite Photocatalysts with Enhanced Performance for the Degradation of Ciprofloxacin, *Mater. Chem. Phys.*, **260**: 124136 (2021).

[56] Chen F., Yang Q., Li X., Zeng G., Wang D., Niu C., Zhao J., An H., Xie T., Deng Y., Hierarchical Assembly of Graphene-Bridged Ag_3PO_4/Ag/$BiVO_4$ (040) Z-Scheme Photocatalyst: An Efficient, Sustainable and Heterogeneous Catalyst with Enhanced Visible-Light Photoactivity Towards Tetracycline Degradation under Visible Light Irradiation, *Appl. Catal. B-Environ.*, **200**: 330 (2017).

[57] Cheng T., Chen C., Wang L., Zhang X., Ye C., Deng Q., Chen G., Synthesis of Fly Ash Magnetic Glass Microsphere@$BiVO_4$ and Its Hybrid Action of Visible-Light Photocatalysis and Adsorption Process, *Pol J Environ Stud*, **30**(3): 2027 (2021).

[58] Zhai Y., Yin Y., Liu X., Li Y., Wang J., Liu C., Bian G., Novel Magnetically Separable $BiVO_4$/Fe_3O_4 Photocatalyst: Synthesis and Photocatalytic Performance under Visible-light Irradiation, *Mater Res Bull*, **89**: 297-306 (2017).

[59] Zhang W., Ma Y., Zhu X., Liu S., An T., Bao J., Hu X., Tian H., Fabrication of Ag Decorated g-C_3N_4/$LaFeO_3$ Z-Scheme Heterojunction as Highly Efficient Visible-Light Photocatalyst for Degradation of Methylene Blue and Tetracycline Hydrochloride, *J. Alloy. Compd.*, **864**: 158914 (2021).

[60] El-Katori E.E., Ahmed M.A., El-Bindary A.A., Oraby A.M., Impact of CdS/SnO_2 Heterostructured Nanoparticle as Visible Light Active Photocatalyst for the Removal Methylene Blue Dye, *J. Photoch. Photobio. A*, **392**: 112403 (2020).

[61] Chandra R., Nath M., Controlled Synthesis of AgNPs@ZIF-8 Composite: Efficient Heterogeneous Photocatalyst for Degradation of Methylene Blue and Congo Red, *J Water Process Eng*, **36**: 101266 (2020).

[62] Nithya M., Vidhya S., Keerthi, A Novel g-C_3N_4/MnV_2O_6 Heterojunction Photocatalyst for the Removal of Methylene Blue and Indigo Carmine, *Chem Phys Lett*, **737**: 136832 (2019).

[63] Xie G., Wang H., Zhou Y., Du Y., Liang C., Long L., Lai K., Li W., Tan X., Jin Q., Qiu G., Zhou D., Huo H., Hu X., Xu X., Simultaneous Remediation of Methylene Blue and Cr(VI) by Mesoporous $BiVO_4$ Photocatalyst under Visible-Light Illumination, *J. Taiwan Inst. Chem. E*, **112**: 357-365 (2020).

[64] Yayapao O., Thongtem T., Phuruangrat A., Thongtem S., Synthesis and Characterization of Highly Efficient Gd Doped ZnO Photocatalyst Irradiated with Ultraviolet and Visible Radiations, *Mat. Sci. Semicon. Proc.*, **39**: 786-792 (2015).

[65] Abd-Elrahim A.G., Chun D.-M., Room-Temperature Deposition of ZnO-Graphene Nanocomposite Hybrid Photocatalysts for Improved Visible-Light-Driven Degradation of Methylene Blue, *Ceram Int*, **47(9)**: 12812-12825 (2021).

[66] Zhang Q., Yu L., Yang B., Xu C., Zhang W., Xu Q., Diao G., Magnetic $Fe3O_4$@Ru-Doped TiO_2 Nanocomposite as a Recyclable Photocatalyst for Advanced Photodegradation of Methylene Blue in Simulated Sunlight, *Chem. Phys. Lett.*, **774**: 138609 (2021).

[67] Chang Y.-C., Lin Y.-W., Lu M.-Y., Construction of MoS_2/ZnO Heterostructures as Highly Efficient Photocatalysts for Enhanced Visible-Light Decomposition of Methylene Blue and Hydrogen Evolution, *Mater. Chem. Phys.*, **266**: 124560 (2021).

[68] Karuppasamy P., Ramzan Nilofar Nisha N., Pugazhendhi A., Kandasamy S., Pitchaimuthu S., An Investigation of Transition Metal Doped TiO_2 Photocatalysts for the Enhanced Photocatalytic Decoloration of Methylene Blue Dye under Visible Light Irradiation, *J. Environ. Chem. Eng.*, **9(4)**: 105254 (2021).

[69] Paul A., Zangrando E., Bertolasi V., Manna S.C., Cu(II)-Na(I) Heterometallic Coordination Compounds as Photocatalyst for Degradation of Methylene Blue, *Inorg. Chim. Acta.*, **522**: 120346 (2021).

[70] Wong K.T., Kim S.C., Yun K., Choong C.E., Nah I.W., Jeon B.-H., Yoon Y., Jang M., Understanding the Potential Band Position and e–/h+ Separation Lifetime for Z-Scheme and Type-II Heterojunction Mechanisms for Effective Micropollutant Mineralization: Comparative Experimental and DFT Studies, *Appl. Catal. B-Environ*, **273**: 119034 (2020).